CFD analysis of the demister location impact on the thermal losses and the vapor uniformity within the MED desalination plant

Ahmed Abotaleb[a],*, Abdelnasser Mabrouk[b,c],*

[a]*Qatar Environment & Energy Research Institute, Hamad Bin Khalifa University, Qatar Foundation, Qatar,*
email: aabotaleb@hbku.edu.qa (A. Abotaleb)
[b]*Qatar Environment & Energy Research Institute, Hamad Bin Khalifa University, Qatar Foundation,*
P.O. Box: 34110 Doha, Qatar, email: aaboukhlewa@hbku.edu.qa (A. Mabrouk)
[c]*College of Science and Engineering, Hamad Bin Khalifa University, Qatar Foundation, Qatar*

ABSTRACT

Several multiple-effect distillation (MED) configurations have been used in the desalination industry. Some configurations classified according to the tube orientation, however, another classified according to the location of the demister whether in the evaporator side or the backside. A lack of computational fluid dynamics (CFD) platform tool to address the effect of the thermal losses within the evaporator and the effect of the vapor flow distribution among tubes on the evaporator performance motivated to development of such CFD tool. This work presents CFD modeling of two commercial MED configurations to identify the optimum tube bundle arrangement and demister location with respect to the evaporator bundle thermal losses, shell volume, footprint as well as minimal operating challenges. The system consists of 620 tubes arranged in a triangular tube pitch either 30° or 60°. Analysis of thermal losses showed that the 60° triangle pitch is optimum for the side demister (MED-SD) evaporator because the 60° arrangement creates a wide passage along the horizontal vapor route which minimizes the pressure drop within tube bundle. On the other hand, the 30° triangle pitch arrangement fits the back demister (MED-BD) evaporator; where a wide vapor passage is created in the downward direction heading to the BD in a lower pressure drop. Moreover, increasing the tube pitch creates wide passages and accordingly smooth flow, hence, less thermal losses. However, increasing the tube pitch will increase both the footprint and shell volume. Furthermore, the vapor velocity distribution at the tube sheet of the MED-BD configuration has a better uniform flow than that of the MED-SD, which indicates that an operational challenge would occur within the MED-SD configuration as some tubes will be admitted by the amount of vapor higher than the design value and accordingly will become overheated.

Keywords: Desalination; MED; Thermal losses; CFD; Evaporator bundle; Triangle tube pitch.

1. Introduction

Thermal desalination still considered as a reliable technology [1], where the seawater characteristic is challenging in terms of high salinity, elevated temperature, high impurity level especially Gulf seawater and sometimes red tide. Thermal desalination, including multi-stage flash (MSF) and multiple-effect distillation (MED) technologies dominate the desalination industry in the Gulf Cooperation Council (GCC) countries, while, the reverse osmosis (RO) membrane

* Corresponding authors.

technology getting a growing market due to its energy efficiency. In Qatar, the thermal desalination dominates 75% of the market, while the rest shared by RO [2]. Among the thermal desalination technologies, the MED operates at lower specific power consumption than the MSF because of using falling film evaporation around tubes (three times of the distillate) instead of pumping a bulk flow of seawater feed (ten times of the product) [2].

Falling film horizontal tubes evaporator is the core technology of the MED desalination process. The evaporation rate depends on the heat transfer kinetics, the tube wall surface characteristics and the falling film seawater properties. The temperature difference between the wall and the falling film is the driving force to increase the evaporation rate [3]. However, this approach enables the nucleate boiling (bubble formation), which ruptures the film evaporation. An expression for the maximum wall temperature prior to bubble formation without the film rupture arising from bubble inception is developed by Mitrovic [3].

The concept of film evaporation has been adopted in the solar still where the evaporation rate likely depends on the water layer thickness. The experimental results showed that solar still production increased by 30% compared to conventional bulk evaporation [4,5]. For the MED desalination technology, the concept of falling film evaporation superseded the bulk evaporation and became the state of the art [6,7]. The generated vapor within the evaporator flows crossover the tubes and intersects with falling film before sweeping from both sides of the tube bundle. At the high vapor velocity region, the vapor velocity might deflect the falling film away from the next tube, which results in an incomplete wetting of the lower tubes. Lorenz et al. [7] determined the falling film angle beyond which the falling film will not wet the lower tube. Based on the tube bundle arrangement and the critical deflection angle, they developed the maximum allowable vapor crossflow velocity. Nevertheless, pressure drops (thermal losses) due to friction loss around tubes generate thermal losses, which increase the required heat transfer area to achieve the product capacity.

A comparison between the square-pitch and triangle-pitch tube bundle [8,9] showed that the average heat transfer coefficient is higher in the square-pitch tube bundle. This explained as in the triangle-pitch bundle the sprayed seawater tends to be less uniform, as cited by previous work by the author in [10], particularly with high heat fluxes. However, on the other hand, the space between tubes in a triangular-pitch bundle is narrower than that of the square-pitch bundle as a result the size of the bundle-based triangle layout is smaller than that based on square layout [10]. The tube bundle arrangement has a considerable influence in the falling film pattern, the wettability criteria and the rate of the scale deposition. The uneven distribution of dripping seawater among tubes in vertical columns in a triangle pitch tube bundle arrangement is simulated and the developed model includes $CaCO_3$ scale formation and CO_2 release [11]. The simulation results showed that the flowrate of the dripping seawater on the column, based on the second row is lower than that of the first row. Consequently, the wetting rate of the tubes in the column based on the second row is less than that on the first row, which explains why the tubes based on

the second-row experience more $CaCO_3$ scale deposit than that on the first row [11].

In addition to that, many studies have presented process simulation (zero-dimension mathematical modeling) of the MED process [12–20], which included empirical correlations for thermal losses occurs within tube bundle, demister, and vapor box. Those equations are used to calculate the available temperature difference. Accordingly, the heat transfer area and sizing the evaporator tube bundle was calculated. The zero-dimensional models focus on the entire system design and performance. However, it does not provide sufficient information about the effect of the tube bundle orientation and the vapor route resistance within the evaporator (tube bundle, demister and vapor box).The numerical computational fluid dynamics (CFD) analysis was conducted to investigate the effect of the velocity variations on the brine carryover factor and the demister pressure drop [21], where the trajectory of liquid droplets associated with the vapor released from tube bundle was calculated using Lagrange approach. A new baffle configuration shows a minimum brine carryover factor of 0.097, while the demister pressure drop is less than 13.4% of the original design.

CFD simulation of the vapor route for two conventional MED configurations named as long tube (MED-LT) and cross tube (MED-CT), respectively are performed by the authors [22]. The CFD results show that that the MED-LT configuration is superior in terms of better vapor uniformity for reliable operation and lower footprint. In both configurations reported in [22], the pressure drop occurs within the tube bundle, demister and the vapor box due to friction, separation and sudden change in the flow path, which expresses the thermal losses within the vapor route are calculated at different recovery ratio. The evaporator tube bundle is responsible for the major thermal losses within the MED system with almost 88%, which actually direct, motivate and encourage the desalination researchers and engineers to exert further efforts focusing on the evaporator tube bundle as a high impact reward component within the MED system. Moreover, it was concluded also that, the vapor uniformity is a crucial parameter, which affects the system performance resulting in dry zones in some tubes, while excessive heating in other tubes [22].

Several MED configurations have been used in the desalination industry. Some configurations classified according to the tube orientation [22], however, another classified according to the location of the demister whether in the evaporator side or in the backside [11,23]. A lack of CFD platform tool to address the effect of the thermal losses within the evaporator and the effect of the vapor flow distribution among tubes on the evaporator performance motivated to development of such CFD tool.

The motivation of this work is to investigate the effect of the demister orientation on the vapor uniformity and thermal losses in two commercial configurations. The aim of this work is to compare between side demister (MED-SD) and back demister (MED-BD) configurations, which have different demister orientation. Using CFD, the two configurations will be simulated to determine thermal losses in the tube bundle, demister, and vapor box. Nevertheless, the CFD enables us to determine the vapor uniformity in the vapor box in both configurations.

2. Description of the MED configurations and methodology

Two existing and commercial MED configurations are shown in Figs. 1a and b [11,23]. The key difference between the two configurations is the location of the demister with respect to the tube bundles. Fig. 1a shows the top view of the MED-SD evaporator configuration in which, the demister is allocated in the side of the evaporator. The generated vapor swept out from both sides of the tube bundle and passed through the horizontal demister. After demister, the vapor moves in parallel to the tube to be collected in the vapor box. As shown in Fig. 1b, the demister is allocated in the back of the evaporator bundle and at the same time exists in the vapor box between two effects. The generated vapor is swept out from the backside of the tube bundle and passed through the horizontal demister. Then, the vapor is induced directly to the next effect.

In this work, the pressure drop in the evaporator vapor route for the two MED configurations will be calculated as well as vapor velocity distribution within the tube bundle, demister and vapor box will be calculated using CFD tool. The previously developed CFD model [22] is used in this comparison analysis, however, the model will be adopted to consider the featured and different geometry aspects of the given two configurations. The pressure drops in the vapor route are mathematically converted to corresponding temperature difference. This temperature difference/loss is reflected in the enthalpy balance as a thermal loss. However, for simplicity, we call this temperature loss as a thermal loss. The thermal losses and vapor uniformity will be calculated for the MED-SD evaporator at two tube triangle pitch angles 60° and 30° where the vapor swept from sides as shown in Figs. 2a and b. Also, the effect of the vapor swept from the

MED-BD on the thermal losses and vapor uniformity will be investigated at 60° and 30° tube pitch angles.

The boundary conditions of the computational domain (one effect working at 50°C) are summarized in Table 1. The heating steam is admitted to the tube bundle at 53°C to be condensed inside the tubes and transfer the latent heat to the sprayed seawater falling film outside the tubes. Part of the falling film is converted as a vapor at 50°C, while the remaining brine is fall in the brine sump at a slightly higher temperature to consider the boiling point elevation. The tube bundle consists of 620 tubes arranged in a triangular tube pitch configuration. The outside tube diameter is 25.4 mm and 1 m length. Demister thickness is 20 mm. It is worth mentioning that, since the heat transfer surface area is fixed by specifying the number of tubes, tube length, and diameter, the recovery ratio is controlled by controlling the feed seawater. While the heat flux inside tubes is fixed, the decreasing of the seawater feed would increase the generated vapor within the tube bundle, that is, increases the process recovery ratio.

The developed CFD simulation determined the outlet boundary conditions at the sides/back of the evaporator tube bundle and used as input boundary conditions (pressure, velocity, temperature) to the demister. Sequentially, the output conditions at the demister are used for the input boundary conditions for the vapor box.

3. Mathematical model

3.1. Model and domain

Steady-state 2D and 3D CFD models are developed for one effect of the MED evaporator using COMSOL Multiphysics v5.3.
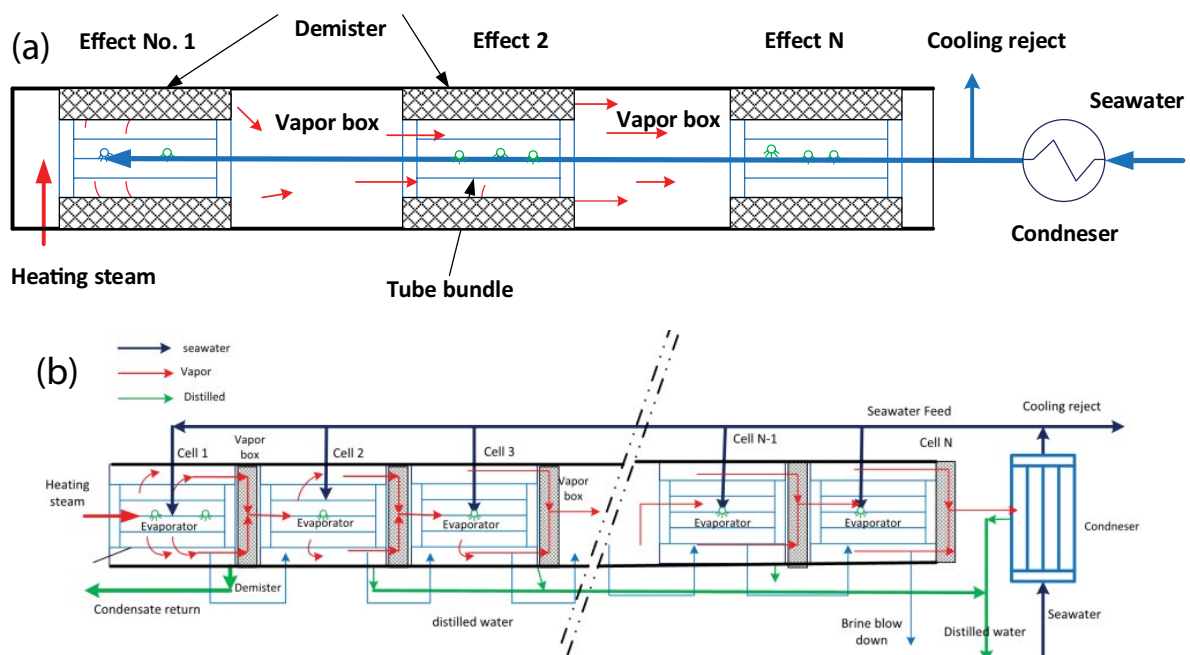

Fig. 1. (a) Top view of side demister evaporator (MED-SD) and (b) top view of back demister evaporator (MED-BD).
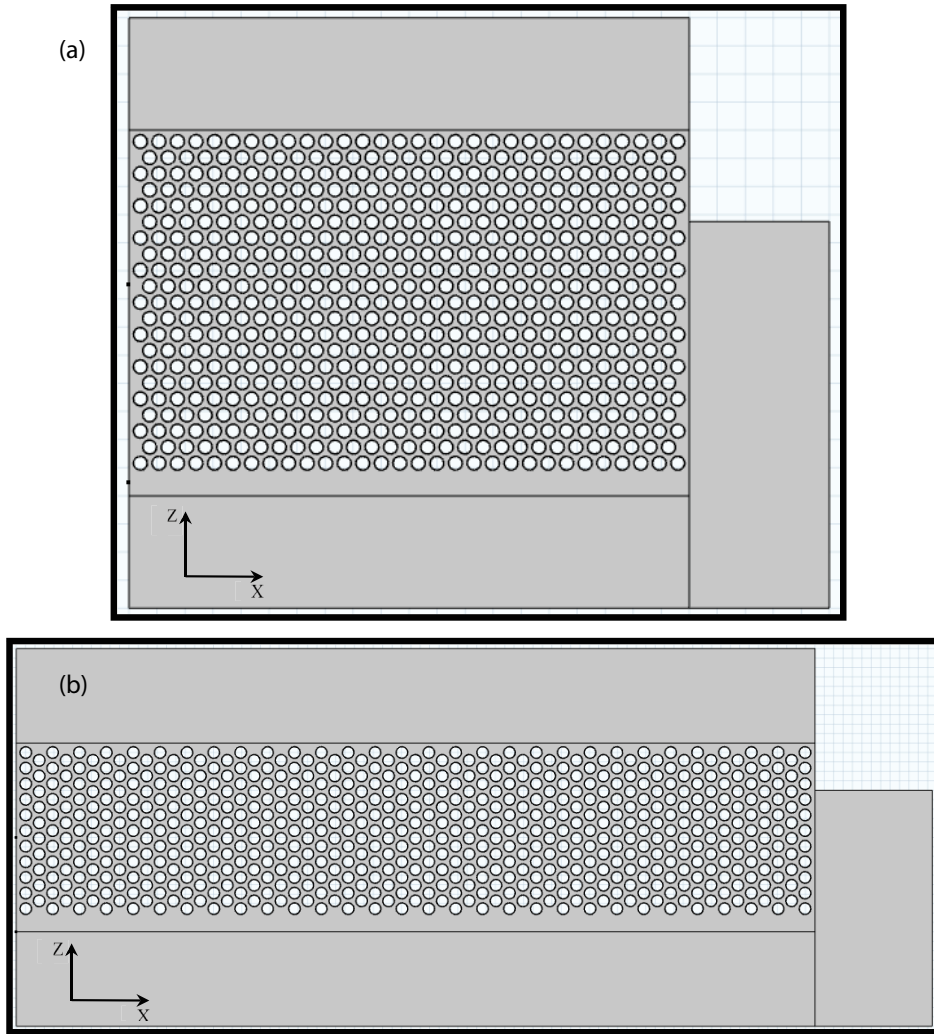
Fig. 2. (a) 60° triangle pitch arrangement for MED-SD at 1.3 tube pitch and (b) 30° triangle pitch arrangement for MED-SD at 1.3 tube pitch.

Table 1
Boundary conditions for one effect of MED evaporator

Parameter	Value	Unit
Falling film flow rate (feed seawater)	3	m³/h
Feed temperature	50	°C
Feed salinity	45	g/L
Inlet vapor temperature	53	°C
Generated vapor temperature	50	°C
Recovery ratio	33	%
No. of tubes	620	
Tube diameter (OD)	25.4	mm
Tube length	1	m
Tube bundle height	0.7	m
Tube bundle width	2	m
Liquid load	0.05–0.1	Kg/ms
System pressure	10–12	mbar
Generated vapor flow	0.3	Kg/s

The mathematical modeling approach has been developed based on the following equations:

Conservation of mass:

$$\frac{\partial \rho}{\partial t} + \nabla(\rho u) = 0 \tag{1}$$

where ρ is the fluid density while u are fluid velocity t is time.

Conservation of momentum:

$$\rho\left[u\frac{\partial u}{\partial x} + v\frac{\partial u}{\partial y} + w\frac{\partial u}{\partial z} \right] = -\frac{\partial P}{\partial x} + \eta\left[\frac{\partial^2 u}{\partial x^2} + \frac{\partial^2 u}{\partial y^2} + \frac{\partial^2 u}{\partial z^2} \right] + \rho g \tag{2}$$

$$\rho\left[u\frac{\partial v}{\partial x} + v\frac{\partial v}{\partial y} + w\frac{\partial v}{\partial z} \right] = -\frac{\partial P}{\partial y} + \eta\left[\frac{\partial^2 v}{\partial x^2} + \frac{\partial^2 v}{\partial y^2} + \frac{\partial^2 v}{\partial z^2} \right] + \rho g \tag{3}$$

$$\rho\left[u\frac{\partial w}{\partial x} + v\frac{\partial w}{\partial y} + w\frac{\partial w}{\partial z} \right] = -\frac{\partial P}{\partial z} + \eta\left[\frac{\partial^2 w}{\partial x^2} + \frac{\partial^2 w}{\partial y^2} + \frac{\partial^2 w}{\partial z^2} \right] + \rho g \tag{4}$$

Transport equations for the standard k-ε model where the turbulent kinetic energy:

$$\frac{\partial}{\partial x_j}\left(\rho k u_j\right) = \frac{\partial}{\partial x_j}\left[\left(\mu + \frac{\mu_t}{\sigma_k}\right)\frac{\partial k}{\partial x_j}\right] + \mu \frac{\partial u_i}{\partial x_j}\left[\frac{\partial u_i}{\partial x_j} + \frac{\partial u_j}{\partial x_i}\right] - \rho\varepsilon \quad (5)$$

Rate of dissipation:

$$\frac{\partial}{\partial x_j}\left(\rho \varepsilon u_k\right) = \frac{\partial}{\partial x_k}\left[\left(\mu + \frac{\mu_t}{\sigma_\varepsilon}\right)\frac{\partial \varepsilon}{\partial x_k}\right] + \frac{c_1 \varepsilon}{k}\mu \frac{\partial u_i}{\partial x_j}\left[\frac{\partial u_i}{\partial x_j} + \frac{\partial u_j}{\partial x_i}\right] - c_2\rho\frac{\varepsilon^2}{k} \quad (6)$$

Figs. 3a and b show 3D geometry of the MED-SD and the MED-BD configurations. Due to symmetrical geometry, it is decided to build half of the domain to save computation time.

The computational domain consists of three zones:

- *Falling film evaporation (tube bundle)*: Steady-state two-dimensional model based on the Euler–Euler laminar flow package is used to calculate the evaporation rate and vapor field around tubes and its movement to sweep out from the bundle. The two-phase pressure drop encountered vapor transportation over tubes is calculated. Two sets of Navier-Stokes equations have been solved, one for each phase, to determine each phase velocity field.
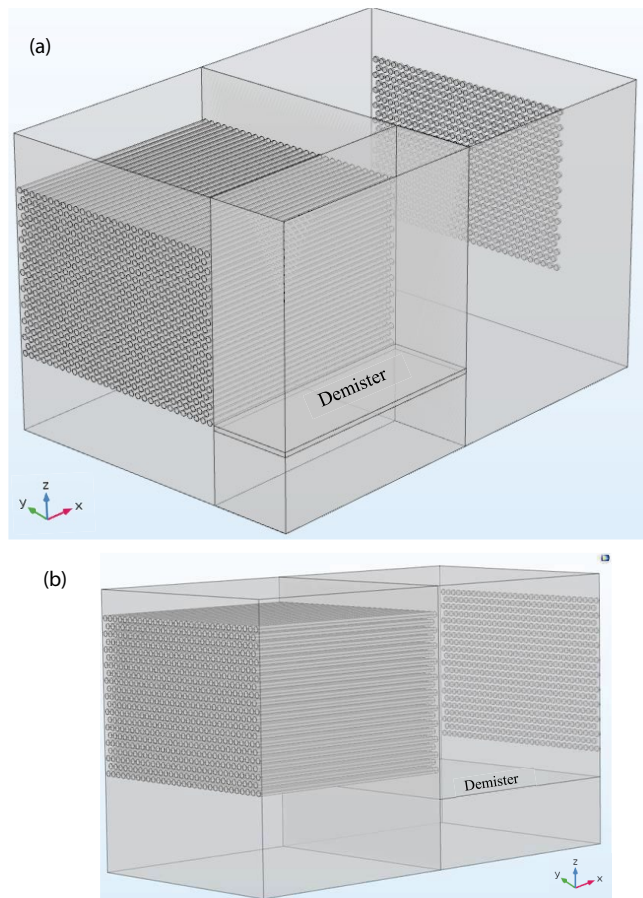

Fig. 3. (a) MED-SD evaporator 3D domain and (b) MED-BD evaporator 3D domain.

The phases interchange momentum is described by a drag model. The pressure is calculated from a mixture-averaged continuity equation and the volume fraction of the dispersed phase is tracked with a transport equation. It's worth mentioning that, there are similar studies used Euler–Euler physics to model two-phase evaporation [22,24–27]. The detailed model of the two-phase flow is presented in Appendix 1

- *Vapor flow through demister*: Steady-state two-dimensional model using Darcy's Law interface to simulate fluid flow through a porous medium at low-velocity flows. The porous medium permeability and porosity are function in the demister design. The pressure gradient is the major driving force and the frictional resistance within the pores mostly influences the flow. It's well known to use Darcy's law in modeling demister/mist eliminator [21,22].

- *Vapor flow through the vapor box*: Steady-state three-dimensional model using non-isothermal turbulent k-ε flow package model is used to model the vapor flow in the domain above demister and the vapor box. The non-isothermal flow calculations are based on coupling the Navier-Stokes equations for conservation of momentum and the continuity equation for conservation of mass. The turbulence effects are modeled using the standard two-equation k-ε model. Flow close to walls is modeled using wall functions. The standard k-ε model was selected due to its robustness and the low computational time compared to another turbulence model for this specific problem [21,22].

3.2. Mesh size and resolution

The used mesh elements are tetrahedral, pyramids, prism, triangular and quadrilateral. Several mesh sizes are considered for the sake of mesh resolution. The studied mesh sizes are (extremely coarse, extra coarse, coarser, coarse, normal and fine). The vapor uniformity standard deviation is calculated at different mesh sizes as shown in Fig. 4. The vapor uniformity standard deviation reaches constantly at 3,000,000 elements (Normal mesh size) and the curve becomes more flattened at 11,000,000 (fine mesh) however it is time-consuming. Compromise between time and acceptable resolution, therefore, the predefined normal mesh size is selected in this study where the total number of elements is 3,016,686 while the element quality of ≈0.78 and minimum element quality is ≈1.64×10^{-6}. The minimum element size has been selected to accurately model the minimum dispersed vapor particle size around the tubes. In addition, the solver convergence termination criteria set at 10^{-5}.

3.3. CFD model verification

The CFD model for two-phase was verified against an empirical correlation: -

The Pressure drop equation for two phases is presented as below [28]:

$$\Delta P = 0.0667\left[\frac{\dot{m}\times\varnothing}{\left(\varnothing-1\right)}\right]^2\frac{n}{\rho} \quad (7)$$
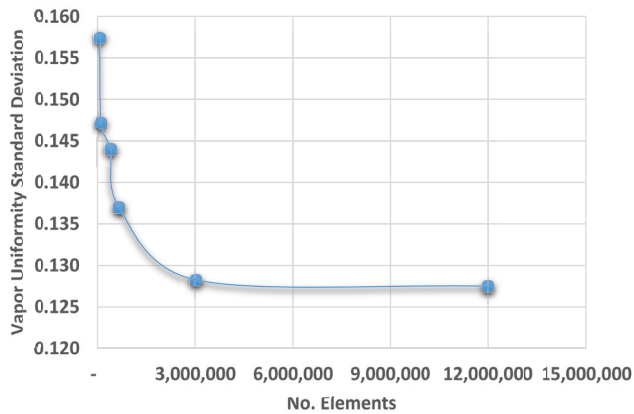
Fig. 4. Vapor uniformity standard deviation variation with the mesh elements [22].

Fig. 5. Pressure drop within tube bundle for CFD model compared to an empirical equation.

where $\dot{m}$ is the vapor mass flow rate; $\varnothing$ is the tube pitch; n is the number of tubes along the vapor route; ρ is the vapor density.

The pressure drops with tube bundle (two-phase) have been extracted from the CFD model are compared with the empirical correlations [28] at different values of tube pitches as shown in Fig. 5. The CFD values are higher than that calculated from the empirical equation and this difference diminish as the tube pitch increase. The comparable higher value of pressure drop extracted from the CFD model is justifiable as the CFD model includes other parameters that aren't considered in the empirical correlations such as the losses results from the entrainment of liquid particles with the vapor flow, the two-phase flow interaction, the kinematic pressure drop as well as considering the local velocity and accordingly the local pressure drop not the average values as considered in the empirical correlations.

The CFD model calculation of the pressure drop in the demister is verified against the empirical equation based on real experiments from a manufacturer as reported in [22,29] and the detailed is presented in Appendix 2.

4. Results and discussion

Using the developed CFD simulation, the velocity distribution in the selected domain is calculated for both configurations and presented as shown in Figs. 6a and b. Hence, the pressure drop is calculated within the tube bundle, demister and the vapor box due to friction, separation and sudden change in the flow path. Afterward, the pressure drop is expressed by temperature loss or thermal losses. The pressure drop within the tube bundle is not only affected by the falling film pattern either columns or droplets but also affected by the friction of crossing vapor over tubes. In fact, as the vapor route becomes longer, the thermal losses get higher (for example, high capacity MED). The vapor route resistance would be also affected by the demister orientation as explained in the below section. The CFD simulation enables calculating the total thermal losses encountered in the tube bundle, demister and the vapor box for both MED-SD and MED-BD configurations at different values of tube-pitch and different angles of tube arrangements.
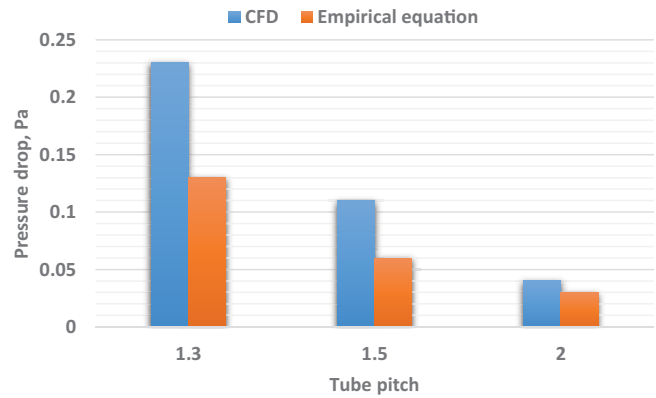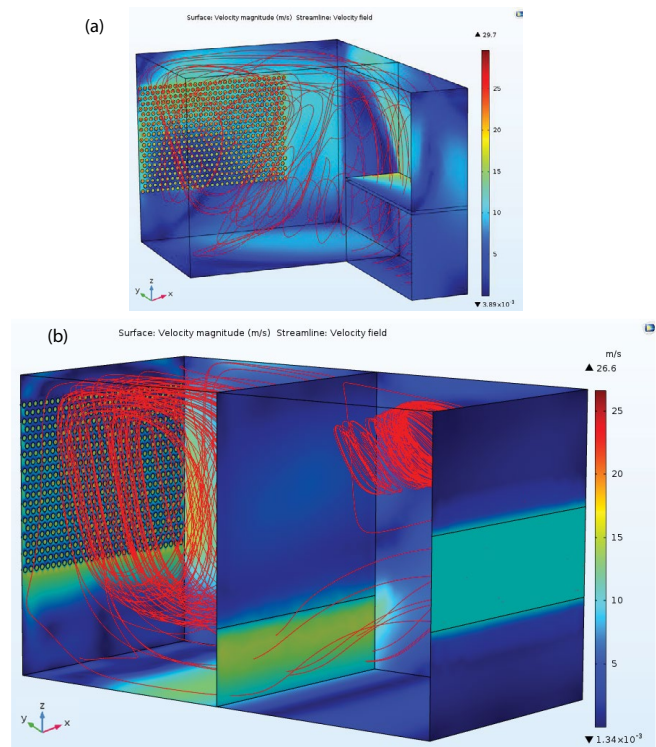

Fig. 6. (a) Vapor velocity distribution for MED-SD, (b) vapor velocity distribution for MED-BD.

As shown in Fig. 7, the pressure drop in the evaporator bundle accounts for 88% of the total pressure drop as it is a result of two-phase flow as well as friction with tube surfaces. The pressure drop in the vapor box accounts for 8% of the total pressure drop. This pressure drop results mainly from the single-phase pressure drop from the demister to the following tube bundle. The pressure drop in the demister accounts for 4% only of the total pressure drop. This pressure drop results mainly from the flow through porous media, where the vapors flow directly, while the liquid droplets stick to the mesh surfaces.

Fig. 8a shows that the thermal losses variations within the MED-SD evaporator at 30° and 60° triangle arrangements
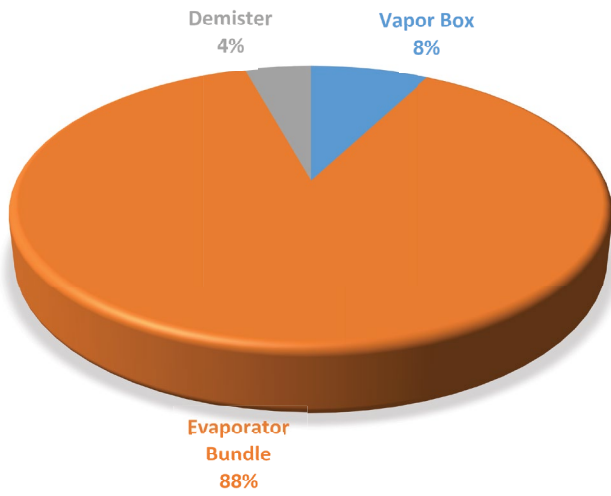
Fig. 7. Fraction of thermal losses in the bundle, demister and vapor box.

Fig. 9. (a) Thermal losses variation at different tube pitches of the MED-BD, (b) 60° triangle pitch with back demister, and (c) 30° triangle pitch with back demister.
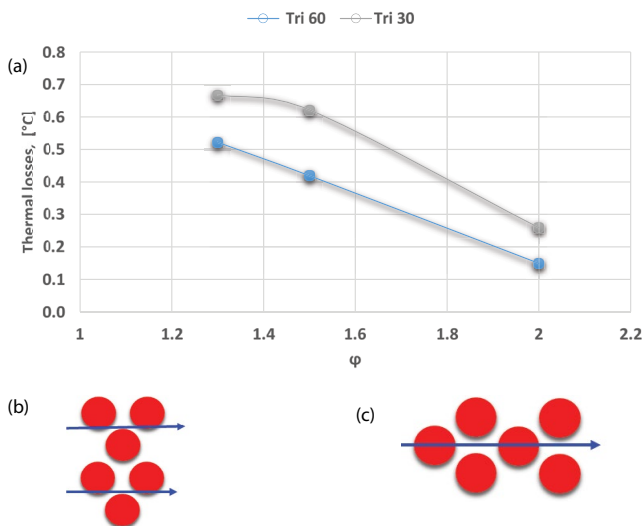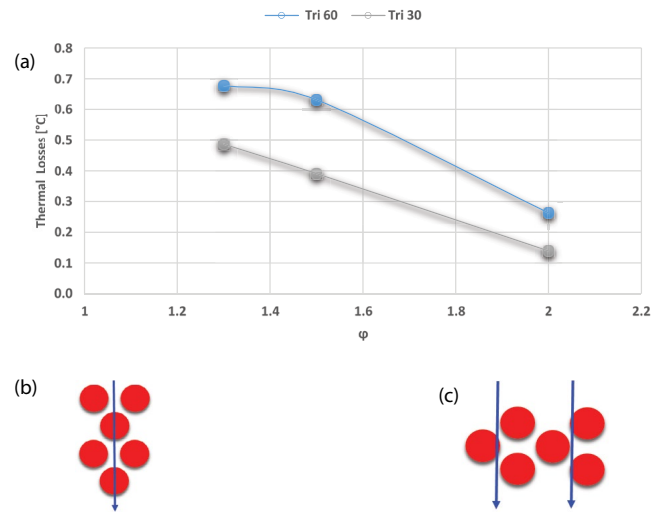

Fig. 8. (a) Thermal losses variation at different tube pitches of the MED-SD, (b) 60° triangle arrangement with side demister, and (c) 30° triangle arrangement with side demister.

and at different values of horizontal tube-pitch. The thermal losses (temperature drop) decrease with increasing the tube pitch for the angle arrangement. The thermal losses at the tube pitch of ($\emptyset = 2$) is 70% lower than that of ($\emptyset = 1.3$). This can be explained at higher tube pitches the passages among tubes are wider which decreases the pressure drop. For the SD, the pressure drop in the tube angle of 60° is almost 42% lower than that of the 30° arrangement. This because in the SD, the generated vapor must exit from the sides and must cross over the tubes until it reach the demister and according to Figs. 8b and c the arrangement of 60° triangle pitch allows a wider passage and route for the vapor while the 30° create a narrow passage and more resistive vapor route.

On the other hand, Fig. 9a shows the thermal losses within the MED-BD evaporator at different values of tube

pitch ($\emptyset$). The thermal losses decrease with increasing the tube pitch because at a large tube pitch the passages among tubes are wider, which decreases the pressure drop. Fig. 8a shows also that for the BD, the pressure drop in the tube angle of 30° is almost 47% lower than that of 60° arrangement. This is because the generated vapor must move parallel to the tubes until they reach the demister at the backside of the tube bundle. From Figs. 9b and c the arrangement 30° allows wide passage to the vapor movement while the 60° create a narrow passage and more resistive vapor route.

From Figs. 8 and 9 it could be concluded that, if the MED-SD evaporator is considered then 60° tube angle would be a viable option however, if MED-BD evaporator is considered then 30° triangle angle arrangement would be better in terms of lower thermal losses. Moreover, increasing the tube pitch gives more space for the vapor for smooth flow, minimizes the deflection rate, minimizes the entrainment and therefore, lower thermal losses. However, increasing the tube pitch will increase both footprint and shell volume.

The shell volume and footprint for all the cases are shown in Figs. 10a, and b, 11a and b, respectively. It's clear that increasing the tube pitch result of increasing the footprint and accordingly the shell volume, which would have a direct impact on the capital cost. On the other hand, increasing the tube pitch leads to lower thermal losses, which lead to either a relatively lower heat transfer area required or higher production capacity. Therefore, a trade-off between the tube pitch, heat transfer area, production capacity, footprint, shell volume and capital cost would decide the optimum tube pitch with reference to the design requirements and/or limitations.

Moreover, it could be concluded for both configurations that, the tube angle of 60° would always have a lower footprint of up to 36% and a lower shell volume up to 10%. The main reason behind that for the 30° tube angle, that the geometry became wider as a horizontal bundle as shown in Fig. 2.
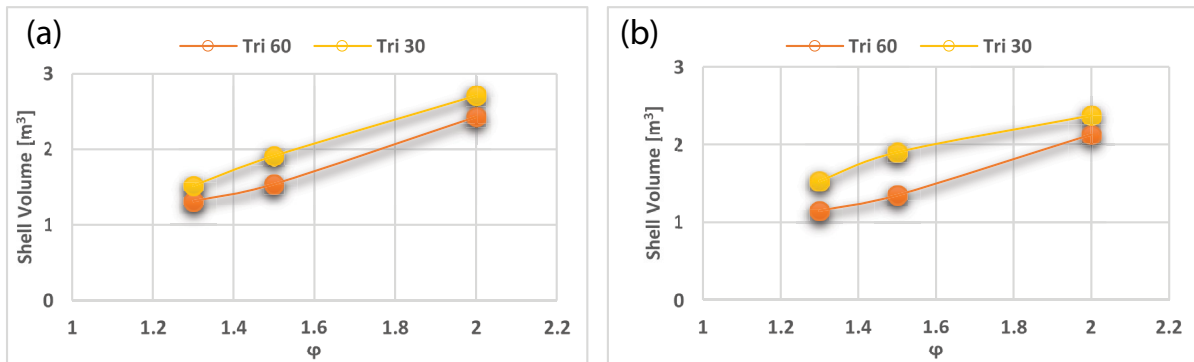
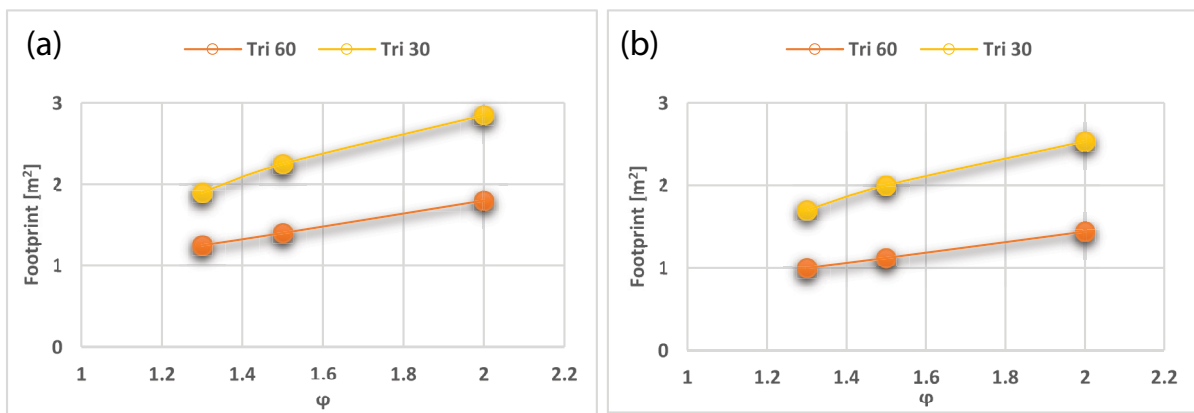Fig. 10. (a) Side demister shell volume and (b) back demister shell volume.

Fig. 11. (a) Side demister footprint and (b) back demister footprint.

On the other hand, the vapor uniformity is considered with the same importance as the thermal losses to ensure the system's production rate, reliability and sustainability. To guarantee accurate findings, the vapor uniformity identification requires a three-dimensional model to detect the flow in the y-axis. Fig. 6a shows the velocity profile along with the streamline's distribution for the SD, while Fig. 6b show BD profile. It can be shown that the BD shows a relatively direct and homogeneous flow with some swirl in the dead areas "Top section, while the SD configuration shows a random flow with many scattered swirls.

This happened due to the geometry of each configuration, wherein the BD configuration, the generated vapor from one effect flows in a straight-way/direct flow heading to the following effect. Therefore, it shows a relatively direct and homogeneous flow. On the other hand, the geometry of the SD configuration forces the generated vapor from one effect to flow in a different and sectional direction. Therefore, it shows a random flow with many scattered swirls.

Figs. 12a and b shows the vapor flow local velocity profile just before entering the following effect for both BD and SD, respectively. It can be concluded that the BD shows a lower turbulence with a maximum velocity of 20.7 m/s, while the SD with 27.8 m/s. Moreover, the back-demister configuration shows almost a uniform vapor distribution compared to the side-demister, which shows dead tubes in some sections. For quantitative analysis, the same

methodology developed by the authors [22] for quantifying the vapor uniformity was used again in this study.

Fig. 13a shows that for MED-SD evaporator, the tube arrangement of 30° is 10% better uniformity than the 60° angular pitch, while Fig. 13b shows that, for BD, the arrangement of 30° triangle pitch is 70% better uniformity than that of 60° triangle pitch.

5. Conclusion

In this work, CFD simulation of the vapor route for two commercial MED configurations; the MED-SD and the MED-BD is performed to determine the thermal losses for (tube bundle, demister, and vapor box) and to determine the vapor uniformity in the vapor box.

CFD results of thermal losses calculation showed that tube angular pitch of 60° is the best fit for MED-SD evaporator. This is because that, the 60° arrangement creates a larger passage along the horizontal vapor route and minimize the pressure drop, while the 30° triangle angle arrangement is the best fit for MED-BD evaporator; this is because the 30° tube angle creates a larger vapor passages in the downward direction, facilitating the vapor movement to reach the BD with lower pressure drop. Moreover, the CFD simulation showed that increasing the tube pitch gives more space and accordingly smooth vapor flow, minimize the deflection rate as well as the entrainment rate. Therefore, lower thermal
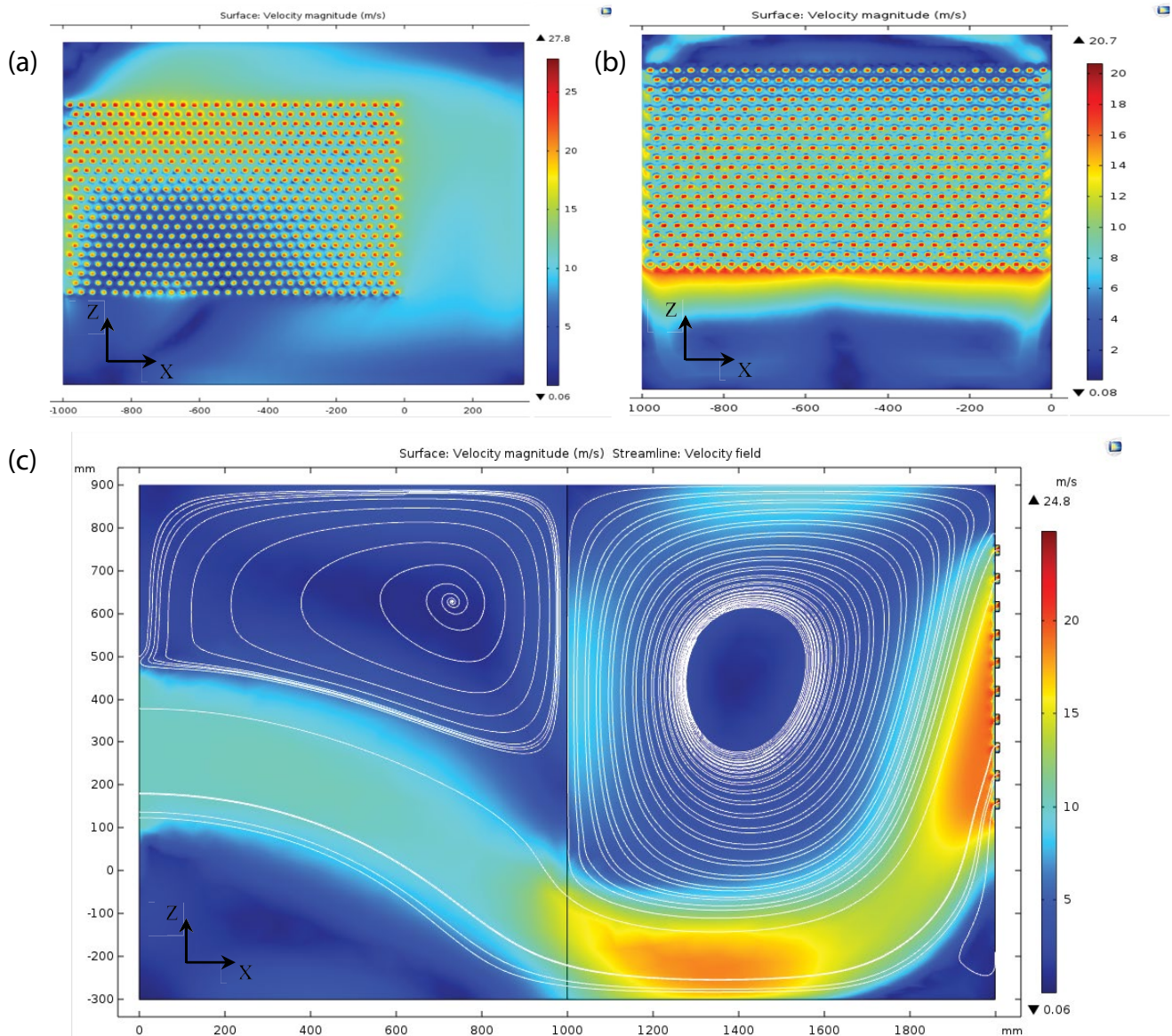
Fig. 12. (a) Velocity magnitude for side demister, (b) velocity magnitude for back demister, and (c) 2D cross section and velocity magnitude for back demister.
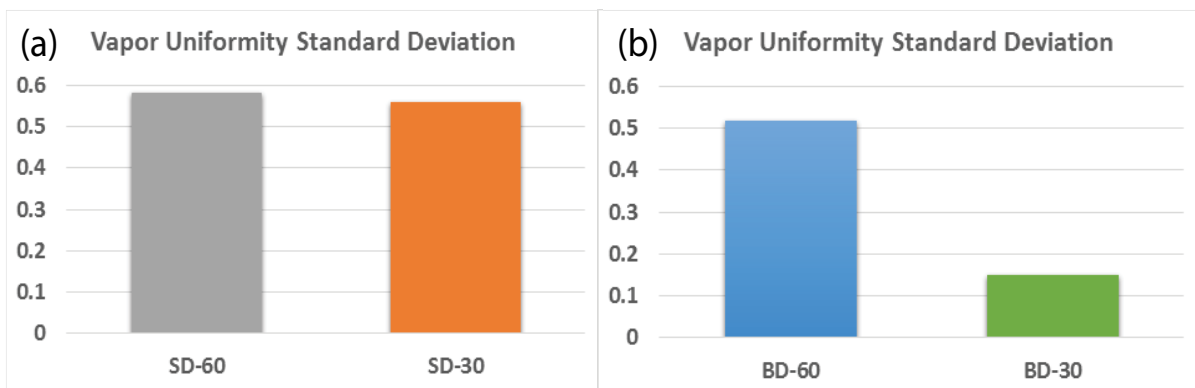

Fig. 13. (a) $\varphi = 1.3$, side demister and (b) $\varphi = 1.3$, back demister.

losses. However, increasing the tube pitch will increase both footprint and shell volume.

The CFD simulation results show that the vapor velocity distribution at the tube sheet where the vapor induced through tubes in the MED-BD has a better uniform flow than that of the MED-SD configuration. This also indicates that a technical challenge would appear within the MED-SD configuration. This is because some tubes will be admitted by the amount of vapor higher than of the design value, and accordingly will become overheated. Also, while seawater falling on the overheated surface, the scale deposition will be formed, which significantly affecting the heat transfer process.

References

[1] IDA Desalination, Yearbook, 2016–2017.
[2] A. Mabrouk, H. Fath, Techno-economic study of a novel integrated thermal MSF-MED desalination technology, Desalination, 371 (2015) 115–125.
[3] J. Mitrovic, Preventing formation of dry patches in seawater falling film evaporators, Desal. Wat. Treat., 29 (2011) 149–157.
[4] A.S. Nafey, M. Abdelkader, A. Abdelmotalip, A.A. Mabrouk, Enhancement of solar still productivity using floating perforated black plate, Energy Convers. Manage., 43 (2002) 576–586.
[5] G. Ribatski, A.M. Jacobi, Falling film evaporation on horizontal tubes-a critical review, Int. J. Refrig., 28 (2005) 635–653.
[6] M. Alhaj, A. Mabrouk, S. Al-Ghamdi, Energy-efficient multi-effect distillation powered by a solar linear Fresnel collector, Energy Convers. Manage., 171 (2018) 576–586.
[7] J.J. Lorenz, D. Yung, E.N. Ganic, Vapor/liquid interaction and entrainment in falling film evaporators, J. Heat Transfer, 77 (1980) 69–73.
[8] B.J. Newton, S.A. Moeykens, M.B. Pate, Effects of surface enhancement film feed-supply rate, and bundle geometry on spray evaporation heat transfer performance, ASHRAE Trans., 101 (1995) 408–419.
[9] J.E. Kelly, S.A. Moeykens, M.B. Pate, Spray evaporation heat transfer performance of R123 in tube bundles, ASHRAE Trans., 102 (1996) 259–272.
[10] M.C. Chyu Zeng, Z.H. Ayub, Experimental investigation on ammonia spray evaporator with triangular-pitch tube bundle, part I: Tube bundle effect, Int. J. Heat Mass Transfer, 44 (2001) 2299–2310.
[11] A. Mabrouk, K. Bourouni, H. Abdulrahim, M. Darwish, A. Sharif, Impacts of tube bundle arrangement and feed flow pattern on the scale formation in large capacity MED desalination plants, Desalination, 357 (2015) 275–285.
[12] H.T. El-Dessouky, H.M. Ettouney, Single effect thermal vapor compression desalination process: thermal analysis, J. Heat Transfer, 20 (1999) 52–68.
[13] J.C. Han, L.S Fletcher, Falling film evaporation and boiling in circumferential and axial grooves on horizontal tubes, Ind. Eng. Chem. Process Des. Dev., 24 (1985) 570–575.
[14] T.A. Adib, B. Heyd, J. Vasseur, Experimental results and modeling of boiling heat transfer coefficients in falling film evaporator usable for evaporator design, Chem. Eng. Process., 48 (2009) 961–968.
[15] K.R. Chun, R.A. Seban, Heat transfer to evaporating liquid films, Trans. ASME: J. Heat Transfer, 93 (1971) 391–396.
[16] A.S. Nafey, H.S. Fath, A.A. Mabrouk. A new visual package for design and simulation of desalination processes, Desalination, 194 (2006) 281–296.
[17] A.S. Nafey, H.S. Fath, A.A. Mabrouk, Thermoeconomic investigation of multi-effect evaporation (MEE) and hybrid multi-effect evaporation-multi stage flash (MEE-MSF) systems, Desalination, 201 (2006) 241–254.
[18] A. Mabrouk, Techno-economic analysis of tube bundle orientation for high capacity brine recycle MSF desalination plants, Desalination, 320 (2013) 24–32.
[19] A. Mabrouk, Techno-economic analysis of once-through long tube MSF process for high capacity desalination plants, Desalination, 317 (2013) 84–94.
[20] A. Mabrouk, H.E.S. Fath, Experimental study of high-performance hybrid NF-MSF desalination pilot test unit driven by renewable energy, Desal. Wat. Treat., 51 (2013) 6895–6904.
[21] M. Mansour, M.A. Qassem, H. Fath, CFD analysis of vapor flow and design improvement in MED evaporation chamber, Desal. Wat. Treat., 56 (2015) 2023–2036.
[22] A. Mabrouk, A. Abotaleb, CFD analysis of the tube bundle orientation impact on the thermal losses and vapor uniformity within the MED desalination plant, Desal. Wat. Treat., 143 (2019) 165–177.
[23] A.A. Mabrouk, A.S. Nafey, H.E. Fath. Thermoeconomic analysis of some existing desalination processes, Desalination, 205 (2007) 354–373.
[24] M. Ayala, P. Santos, G. Hamester, O. Ayala, Secondary Flow of Liquid–Liquid Two-Phase Fluids in a Pipe Bend, Proc. COMSOL Conference in Boston, 2016.
[25] N.G. Deen, M. Annal, J.A.M. Kuipers, Multi-scale modeling of dispersed gas–liquid two-phase flow, Chem. Eng. Sci., 59 (2004) 1853–1861.
[26] A.A. Mostafa, H.C. Mongia. On the modeling of turbulent evaporating sprays: Eulerian vs. Lagrangian approach, Int. J. Heat Mass Transfer, 30 (1987) 2583–2593.
[27] T.H. Nigim, J.A. Eaton, CFD prediction of flashing processes in a MSF desalination chamber, Desalination, 420 (2017) 258–272.
[28] M. Rowe, B.J. Davidson, E.F.C. Andrews, J.A. Ferrison, B.J. Taylor, Heat transfer and air blanketing in steam condenser, Proc. Conf. on Steam Turbines for the 1980s, Institution of Mechanical Engineers, London, 1979, pp. 153–162.
[29] http://hanbal.kr/pdf/hanbal.pdf.

Appendix

A1. Model of two-phase flow

It was mentioned in our previous paper [22].
Here are the equations:
Continuity equations

$$\frac{\partial}{\partial t}\left(\rho_m\right) + \nabla\left(\rho_m\vec{\upsilon}_m\right) = \dot{m} \tag{A1}$$

Mass-averaged velocity

$$\vec{\upsilon}_m = \frac{\sum\limits_{k=1}^{n}\alpha_k\rho_k\vec{\upsilon}_k}{\rho_m} \tag{A2}$$

Density mixture

$$\rho_m = \sum\limits_{k=1}^{n}\alpha_k\rho_k \tag{A3}$$

Momentum equation for each phase

$$\frac{\partial}{\partial t}\left(\rho_m\vec{\upsilon}_m\right) + \nabla\left(\rho_m\vec{\upsilon}_m\vec{\upsilon}_m\right) = -\nabla p + \nabla\left[\mu_m\left(\nabla\vec{\upsilon}_m + \nabla\vec{\upsilon}_m^T\right)\right] +$$
$$\rho_m\vec{g} + \vec{F} + \nabla\left(\sum\limits_{k=1}^{n}\alpha_k\rho_k\vec{\upsilon}_{dr,k}\vec{\upsilon}_{dr,k}\right) \tag{A4}$$

Viscosity mixtures

$$\mu_m = \sum\limits_{k=1}^{n}\alpha_k\mu_k \tag{A5}$$

Secondary phase drift velocity

$$\vec{\upsilon}_{dr,k} = \vec{\upsilon}_k - \vec{\upsilon}_m \tag{A6}$$

Energy equation

$$\frac{\partial}{\partial t}\sum\limits_{k=1}^{n}\left(\alpha_k\rho_k E_k\right) + \nabla\sum\limits_{k=1}^{n}\left(\alpha_k\vec{\upsilon}_k\left(\rho_k E_k + p\right)\right) = \nabla\left(k_{eff}\nabla T\right) + S_E \tag{A7}$$

where k_{eff} is the effective conductivity $(k + k_t)$, where k_t is the turbulent thermal conductivity. The first term on the right-hand side represents energy transfer due to conduction. S_E includes any other volumetric heat sources.

For a compressible phase, and $E_k = h_k$ for an incompressible phase, where h_k is the sensible enthalpy for phase k.

$$E_k = h_k - \frac{p}{\rho_k} + \frac{\upsilon_k^2}{2} \tag{A8}$$

Relative velocity

$$\vec{\upsilon}_{pq} = \vec{\upsilon}_p - \vec{\upsilon}_q \tag{A9}$$

The relative velocity (also referred to as the slip velocity) is defined as the velocity of a secondary phase (p) relative to the velocity of the primary phase (q).

Volume fraction of the secondary phase.

From the continuity equation for secondary phase p, the volume fraction equation for secondary phase p can be obtained:

$$\frac{\partial}{\partial t}\left(\alpha_p\rho_p\right) + \nabla\left(\alpha_p\rho_p\vec{\upsilon}_m\right) = -\nabla\left(\alpha_p\rho_p\vec{\upsilon}_{dr,p}\right) \tag{A10}$$

A2. Pressure drops in the demister

The computational fluid dynamics (CFD) model calculation of the pressure drop in the demister is verified against the empirical equation based on real experiments from a manufacturer as reported in [29] and presented in the author previous work [22].

(d)
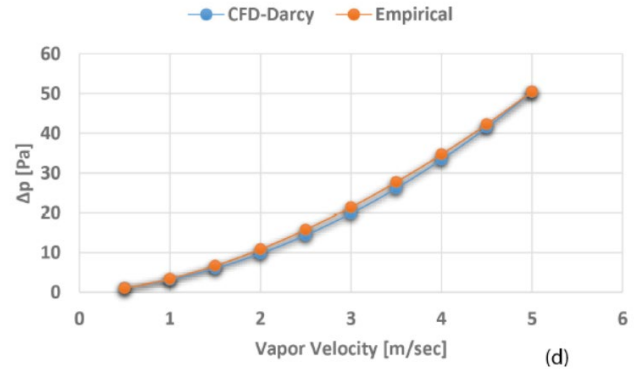
There is a good agreement between the CFD model and the manufacture equation as shown in the above graph with average error of ±5%.

Pressure drop in the demister, the manufacturer equations along with demister main parameters are shown below:

$$\Delta p = \frac{f \times t \times \left(1 - \varepsilon_v\right) \times \rho_v \times v_{max}^2}{D_w} \tag{A11}$$

$$f = 5.3\left(\frac{\rho_v \times v_{max}^2 \times D_w}{\mu_v}\right)^{-0.32} \tag{A12}$$

$$v_{max} = k\frac{\sqrt{\left(\rho_l - \rho_v\right)}}{\rho_v} \tag{A13}$$

$$v_{optimum} = 0.8 v_{max} \tag{A14}$$

where t is the demister thickness, 0.15 m; ε_v is the void fraction "porosity", 0.98; D_w is the wire diameter, 0.0003 m; k is the demister coefficient, 0.108; v_{max} is the maximum allowable vapor velocity; $v_{optimum}$ is the optimum operational vapor velocity.

The demister is a porous media over a definite thickness where the accounted pressure change is identified as a combination of Darcy's law and the inertial loss term as the follow:

$$\Delta p = t\left(\frac{v\mu_v}{\alpha} + \frac{C_2\rho_v v^2}{2}\right) \tag{A15}$$

$$\alpha = \frac{D_w^2\varepsilon_v^3}{150(1-\varepsilon_v)^2} \tag{A16}$$

$$C_2 = \frac{3.5(1-\varepsilon_v)}{D_w^2\varepsilon_v^3} \tag{A17}$$

where α is the permeability; C_2 is the pressure jump coefficient.